

Supplementary Materials for

A highly stretchable, transparent, and conductive polymer

Yue Wang, Chenxin Zhu, Raphael Pfattner, Hongping Yan, Lihua Jin, Shucheng Chen, Francisco Molina-Lopez, Franziska Lissel, Jia Liu, Noelle I. Rabiah, Zheng Chen, Jong Won Chung, Christian Linder, Michael F. Toney, Boris Murmann, Zhenan Bao

Published 10 March 2017, *Sci. Adv.* **3**, e1602076 (2017)

DOI: 10.1126/sciadv.1602076

The PDF file includes:

- section S1. Selection of STEC enhancers
- section S2. Mechanical characterization of bulk freestanding films
- section S3. Effect of STEC on PEDOT:PSS
- section S4. Morphology of PEDOT/STEC film interior
- section S5. Microscopy study of the effect of tensile strain on PEDOT/STEC films
- section S6. Electrical properties of PEDOT/STEC films
- section S7. Composition of PEDOT/STEC films
- section S8. Low-temperature measurements
- section S9. FoM for transparent conductors
- section S10. Testing geometry for PEDOT films under tensile strain
- section S11. Polarized UV-vis-NIR spectra for PEDOT films under tensile strain
- section S12. Cycling stability and morphological change of PEDOT with STEC additives
- section S13. Mixed ion-electron conductivity
- section S14. PEDOT/STEC as interconnects for FET arrays
- table S1. Summary of STEC structures and their effects on the electrical and mechanical properties of freestanding PEDOT:PSS films (thickness range, 150 to 200 μm) with 45.5 wt % of STEC.
- table S2. Summary of mobility and threshold voltage shift for the 3×3 transistor arrays under 0 and 125% strain.
- fig. S1. Plot summarizing the conductivity, maximum tensile strain, and Young's modulus for freestanding PEDOT:PSS films ($\sim 150 \mu\text{m}$ in thickness) with all additives investigated in this paper.

- fig. S2. Mechanical characterization of bulk freestanding films.
- fig. S3. Mechanism behind STEC-induced morphology change for PEDOT:PSS films.
- fig. S4. AFM phase images of PEDOT with various additives.
- fig. S5. GIWAXS analyses of PEDOT films.
- fig. S6. Diffraction data for PSS and insoluble PEDOT control samples.
- fig. S7. Plasticizing effect of STEC on PEDOT and NaPSS individually.
- fig. S8. SEM characterization of the cross section of a stretchable PEDOT film.
- fig. S9. Optical microscope images of a PEDOT/STEC1 film supported on a SEBS substrate under various strains.
- fig. S10. Optical microscope images of a PEDOT/STEC1 film supported on a SEBS substrate after being stretched to various strains and returned to its original length.
- fig. S11. Surface profile analyses of PEDOT films after stretching.
- fig. S12. Optical microscope images of a PEDOT/STEC1 film upon unloading from 100% strain.
- fig. S13. Optical microscope images of a PEDOT/STEC2 film held under various tensile strains.
- fig. S14. Optical microscope images of a PEDOT/STEC2 film upon stretching to various tensile strains.
- fig. S15. Conductivity values of PEDOT/STEC films processed under different conditions.
- fig. S16. Conductivity of PEDOT/STEC films with various STEC weight % before and after further STEC solution treatment.
- fig. S17. Effect of further doping using STEC solution on spin-coated films.
- fig. S18. Chemical composition of PEDOT/STEC films.
- fig. S19. Temperature-dependent conductivity and first- and second-order temperature coefficients for PEDOT films.
- fig. S20. Arrhenius plots for temperature dependent conductivity.
- fig. S21. Schematic diagrams of tensile testing and conductivity measurement geometries.
- fig. S22. Tension-induced chain-alignment behavior of PEDOT/STEC films.
- fig. S23. XPS analysis of film surfaces under 0% versus 100% strain, after returning from 100% to 0% strain, and after 1000 stretching cycles to 100% strain.
- fig. S24. Cycling stability of PEDOT/STEC1 films.
- fig. S25. Cycling stability of PEDOT/STEC2 films.
- fig. S26. Mixed ion-electron conductivity measurements.
- fig. S27. Schematic showing the cross-sectional view of a linear rigid-island array connected with stretchable PEDOT.
- fig. S28. Schematic diagrams illustrating strain calculation for rigid-island devices.
- fig. S29. Schematic and transfer characteristics for a 3×1 FET array.
- fig. S30. Schematic and transfer characteristics for a 3×3 FET array.
- fig. S31. A 3×3 FET array being stretched on a spherical object.

Other Supplementary Material for this manuscript includes the following:
(available at advances.sciencemag.org/cgi/content/full/3/3/e1602076/DC1)

- video S1 (.mov format). A stretchable LED device poked with a sharp object.
- video S2 (.mov format). Twisting and stretching of a stretchable LED device.
- video S3 (.mov format). A 3×3 FET array stretched on a spherical object.

Supplementary Materials

section S1. Selection of STEC enhancers

In order to increase the stretchability of PEDOT:PSS, plasticizers such as Zonyl or Triton needs to be incorporated. PEDOT becomes more stretchable with a higher plasticizer concentration; however, the increase in plasticizer (an insulator) concentration usually causes the conductivity to decrease, which poses as a significant issue for their application as electrodes or interconnects.

We found that a variety of small molecule ionic additives can serve as effective STECs for PEDOT:PSS for inducing both high stretchability and high conductivity. Their ionic nature allowed them to simultaneously tune morphology and dope the polymer, while also promoting effective phase separation between PEDOT and PSS and enhancing the crystallinity of the PEDOT-rich domains (mechanism and selection guideline discussed in main text and Supplemental Section 2). Figure S1 summarizes the key bulk material characteristics: conductivity, maximum tensile strain, and Young's modulus, for free-standing films that are approximately 200 μm thick. We chose the additives that lead to conductivity over 100 S/cm and a maximum tensile strain above 100%, STEC1-3, for further investigation. The names and structures of the additives are shown in table S1.

The conductivity values for these thick drop-casted films are lower than those of the thin spin-coated films presented in Fig. 4a and figs. S15 and S16. This is a general phenomenon that has been observed for PEDOT:PSS films (*Appl. Phys. Express* 2016, **9**(5): 051601). This difference is attributed to morphology difference due to processing methods and drying kinetics. Additionally, in this work, the spin-coated films were further rinsed with STEC solution while the drop-casted films were not further treated. Note that the free-standing films were necessary for mechanical property testing, and their conductivities measured to serve as a guide for us to identify the most suitable STEC additives among the large amount of possibilities (table S1 and fig. S1). STEC1, 2,

3 were identified as the highest performing STEC, and their electrical properties were further enhanced and studied in detail (Fig. 4a and figs. S15 and S16).

table S1. Summary of STEC structures and their effects on the electrical and mechanical properties of freestanding PEDOT:PSS films (thickness range, 150 to 200 μm) with 45.5 wt % of STEC.

#	STEC Structure	Chemical name	Freestanding PEDOT:PSS film with STEC additive		
			Conductivity (S/cm)	Maximum tensile strain (%)	Young's modulus (MPa)
1		Bis(trifluoromethane)sulfonimide lithium salt	608	133	55
2		4-(3-Butyl-1-imidazolium)-1-butanesulfonic acid triflate	420	112	28
3		1-Butyl-3-methylimidazolium octyl sulfate	288	176	47
4		Zinc di[bis(trifluoromethylsulfonyl)imide]	805	58	176
5		4-(3-Butyl-1-imidazolium)-1-butanesulfonate	3.4	136	34
6		1-Ethyl-3-methylimidazolium bis(trifluoromethylsulfonyl)imide	720	71	141
7		Methyl-trioctylammonium bis(trifluoromethylsulfonyl)imide	292	22	706
8		Trihexyltetradecyl phosphonium bis(2,4,4-trimethylpentyl)phosphinate	0.3	16	1365
9		1-Butyl-3-methylpyridinium bis(trifluoromethylsulfonyl)imide	21	5	636
10		Dioctyl sulfosuccinate sodium salt	42	41	178
11		Sodium dodecylbenzenesulfonate	128	54	277
12		Dodecylbenzenesulfonic acid	542	56	151

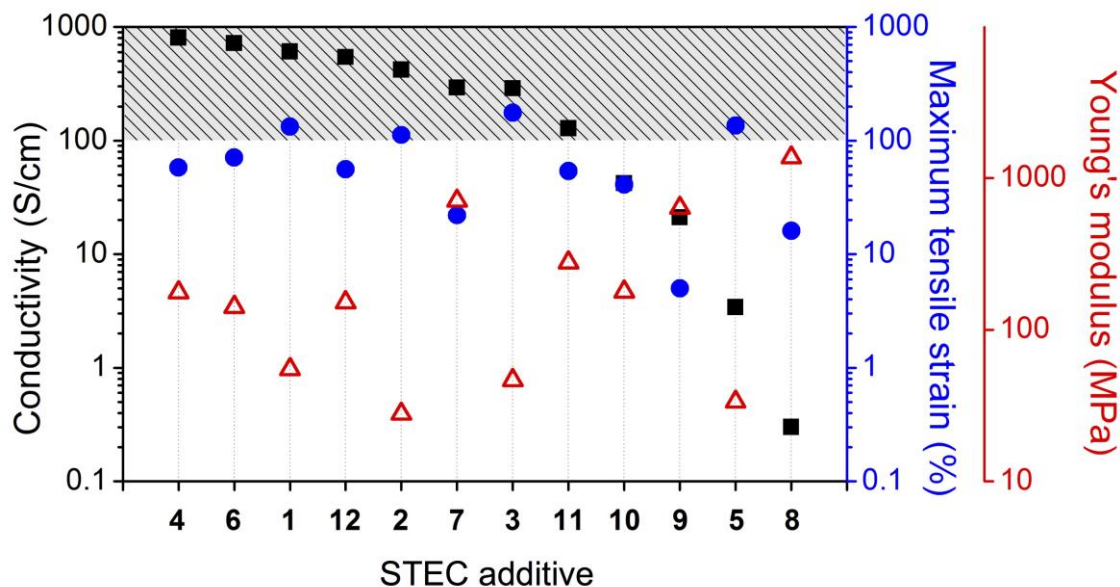


fig. S1. Plot summarizing the conductivity, maximum tensile strain, and Young's modulus for freestanding PEDOT:PSS films (~150 μm in thickness) with all additives investigated in this paper. The additives (STEC1, 2, and 3) that simultaneously led to conductivity above 100 S/cm and maximum tensile strain over 100% were chosen for detailed investigation. The trends in these three parameters reveal that additives with bulky, long hydrocarbon side chains such as STEC7-9 do not plasticize PEDOT:PSS to a significant extent due to their high hydrophobicity. The mixtures have high Young's moduli and low maximum tensile strains. Anions such as bis(trifluoromethylsulfonyl) imide (TFMSI) or triflate are highly acidic, and hence serve as effective dopants for PEDOT. Additives containing such anions, such as STEC1, 2, 4, 6 and 7, lead to highly conductive PEDOT:PSS films even with up to 45.5 wt% STEC, while less acidic dopants like phosphinate (STEC8) result in no conductivity enhancement. Note that although the anion of STEC9 is also TFMSI, the high hydrophobicity of the pyridinium cation limits its solubility in water, hence has minimal effect on film conductivity.

section S2. Mechanical characterization of bulk freestanding films

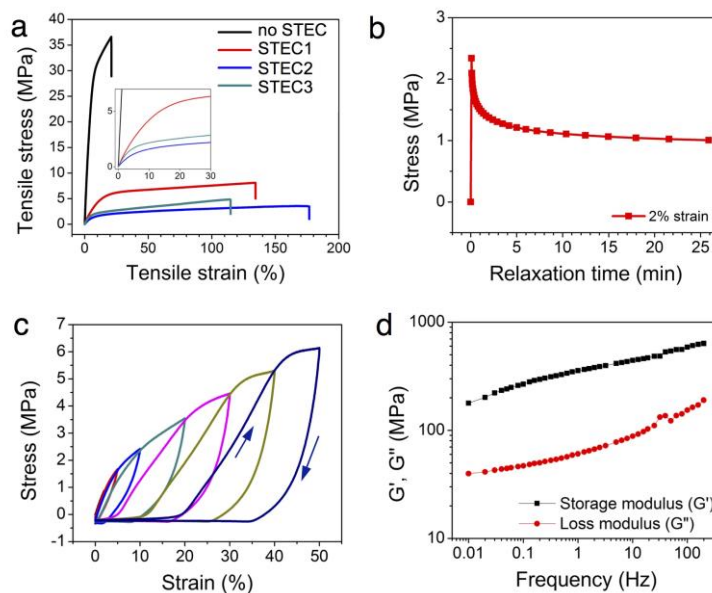


fig. S2. Mechanical characterization of bulk freestanding films. (a) Stress/strain behavior of freestanding PEDOT films with various additives. Inset provides a zoomed-in view over the lower strain section where the elastic-to-plastic transition occurs. (b) Stress relaxation, (c) Strain cycling (arrows indicating loading and unloading paths) and (d) storage and loss moduli of PEDOT/STEC2 films.

To elucidate the mechanical properties of the stretchable PEDOT, the stress/strain behavior of the free-standing films with various STEC additives are compared to the control sample without STEC but with DMSO, a common polar additive for enhancing PEDOT:PSS conductivity (*Displays* 2013, **34**(5): 423-436), was studied (Fig. 1f). The control film ruptures when 18% strain was applied, confirming previous reports that conventional PEDOT has poor stretchability (*Adv. Funct. Mater.* 2012, **22**(2): 421-428). On the other hand, the PEDOT films with STEC additives 1, 2, 3 have greatly enhanced maximum tensile strain of 133%, 112%, and 176%, respectively (Fig. 1f). This enhancement in stretchability is attributed to a combination of the fibrous morphology (Fig. 3, h to k) and the plasticizing effect of STEC molecules in the disordered domains in PEDOT:PSS (Supplementary Section 3c). The most stretchable films mostly possess fibrous morphology (Fig. 3, h to k and fig. S4), which could be a significant contributing

factor for achieving high stretchability, as proposed by previous studies (*Adv. Funct. Mater.* 2015, **25**(3): 427-436).

To confirm the plasticizing effects of STEC on PEDOT:PSS, STEC2 was separately mixed with NaPSS and insoluble PEDOT as a model system (fig. S7). Incorporating 45.5 and 62.5 wt% of STEC2 into the insoluble, powdery PEDOT lead to a paste and gel-like substance, respectively, suggesting the STEC can effectively swell PEDOT chains (fig. S7, a to d) (*Science* 2008, **321**(5895): 1468-1472). Mechanical tests could not be carried out since the paste does not possess good film forming properties, likely due to the low molecular weight of PEDOT. On the other hand, including STEC2 into NaPSS led to a significant increase in stretchability and a much reduced Young's modulus, illustrating the plasticizing effect of STEC for PSS (fig. S7e). Therefore, due to the ability of STECs to serve as effective plasticizers for both PEDOT and PSS, STEC addition led to significantly enhanced maximum tensile strains and reduced Young's moduli.

To further characterize the mechanical properties of the PEDOT/STEC films, stress relaxation, strain cycling, and frequency sweep experiments were carried out (fig. S2, b to d). A relaxation time of approximately 72 seconds was measured (fig. S2b). We loaded and unloaded a PEDOT/STEC film with a strain rate of 0.1/min and reloaded the sample to a larger strain after waiting for 5 min between two cycles (fig. S2c). The stress-strain curves showed hysteresis between loading and unloading. When the film was stretched beyond 20% strain, the film length change became only partially reversible, indicating the viscoplastic response of the film. In the frequency sweep experiment shown in fig. S2d, the storage modulus is higher than the loss modulus during the entire frequency range, confirming the film is a solid rather than a fluid despite the high concentration of STEC. SEM analysis of the film cross-section also shows a densely packed, solid interior (fig. S8, a to b).

section S3. Effect of STEC on PEDOT:PSS

The STEC additives have three effects on PEDOT:PSS: (a) inducing phase separation forming distinctive PEDOT- and PSS-rich domains; (b) enhancing the crystallinity of the PEDOT-rich domains; (c) plasticizing the amorphous regions of PEDOT and PSS.

(a) Effect on phase separation and morphology

Previous literature proposed that the Clevios PEDOT:PSS PH1000 dispersion that we used in this study has a core-shell structure (*Displays* 2013, **34**(5): 423-436). PSS is water soluble, and the sulfonate groups serve as dopants for the conductive PEDOT. The low molecular weight PEDOT (MW ~1000-2500 Da) is insoluble in water; hence, it adheres to segments of the high molecular weight PSS chains (MW ~400,000 Da) through Coulombic attractions. These ionic complexes form coiled, globular structures in water where the hydrophilic PSS-rich shell shields the hydrophobic PEDOT-rich core from water, forming a colloidal dispersion. However, the insulating PSS shells become a barrier for charge transport between the PEDOT-rich domains, resulting in low conductivity (<1 S/cm) in films.

Previous reports have suggested that polar or ionic substances such as ethylene glycol or ionic liquid can induce the merging of PEDOT/PSS particles (fig. S3a) (*Displays* 2013, **34**(5): 423-436; *Macromolecules* 2008, **41**(16): 5971-5973). When STEC molecules such as STEC are incorporated into the PEDOT:PSS system, due to their small sizes, they can more easily interact with both the positively-charged PEDOT and the negatively-charged PSS chains. This leads to a charge screening effect that weakens the Coulombic interactions between the PEDOT and PSS chains. Therefore, larger PEDOT-rich domains can form due to the dissociation between some PEDOT and PSS, which aids in enhancing the conductivity of the films (*Displays* 2013, **34**(5): 423-436; *Adv. Funct. Mater.* 2012, **22**(13): 2723-2727). In fact, dynamic light scattering profiles (fig. S3b) show that the average particle sizes of the PEDOT:PSS colloids increase significantly

upon the addition of various STEC additives, confirming the mechanism depicted in fig. S3a.

This STEC-induced charge screening effect is also reflected by the AFM images of the solid films (fig. S4). The PEDOT:PSS film with 5% DMSO and without STEC enhancers show a rather featureless morphology (fig. S4a). However, clear domains of larger feature sizes are formed with the addition of any of the STEC enhancers (fig. S4, b to j). Note that the morphology of the films is not the sole factor in determining the film conductivity. fig. S4, c to f illustrate the four most conductive PEDOT/STEC systems, while fig. S4b corresponds to a film that is poorly conductive (0.3 S/cm). One possible reason responsible for the low conductivity is that the PEDOT-rich grains in PEDOT/IL8 do not appear to be well-connected, hence leading to a poor conduction pathway. The precise mechanism is still under investigation.

The STEC-induced charge screening can also have an effect on the chain conformation of polyelectrolyte complexes such as PEDOT:PSS (*Displays* 2013, **34**(5): 423-436). The weakened Coulombic interaction between PEDOT and PSS allows PEDOT to be partially dissociated from the highly coiled PSS and adopt a more planar conformation, which promotes delocalization of charge carriers that can lead to an increase in conductivity. Raman spectra of the PEDOT/STEC films show a red shift of the $C_{\alpha}=C_{\beta}$ vibration peak ($\sim 1445\text{ cm}^{-1}$) and narrowing of the peak compared to the PEDOT without any additives (Fig. 3a). This change indicates that a higher proportion of the resonant structure of PEDOT chains is turning from the benzoid structure in the pure PEDOT:PSS films to the more planar quinoid structure in PEDOT/STEC (*Macromolecules* 2009, **42**(12): 4141-4147; *Adv. Funct. Mater.* 2005, **15**(2): 203-208; *Synth. Met.* 2001, **125**(3): 325-329). In addition, compared to the plain PEDOT:PSS films, UV-vis-NIR spectra of the PEDOT/STEC films exhibit a more prominent free-carrier tail that extends into NIR and a less well-defined peak around 800 nm. Such results suggest better delocalization of charges along the PEDOT backbone (*Synth. Met.* 2000, **110**(1): 79-83; *Solid State Commun.* 1986, **59**(7): 415-421), another indication for a less coiled chain conformation, which leads to enhanced conductivity.

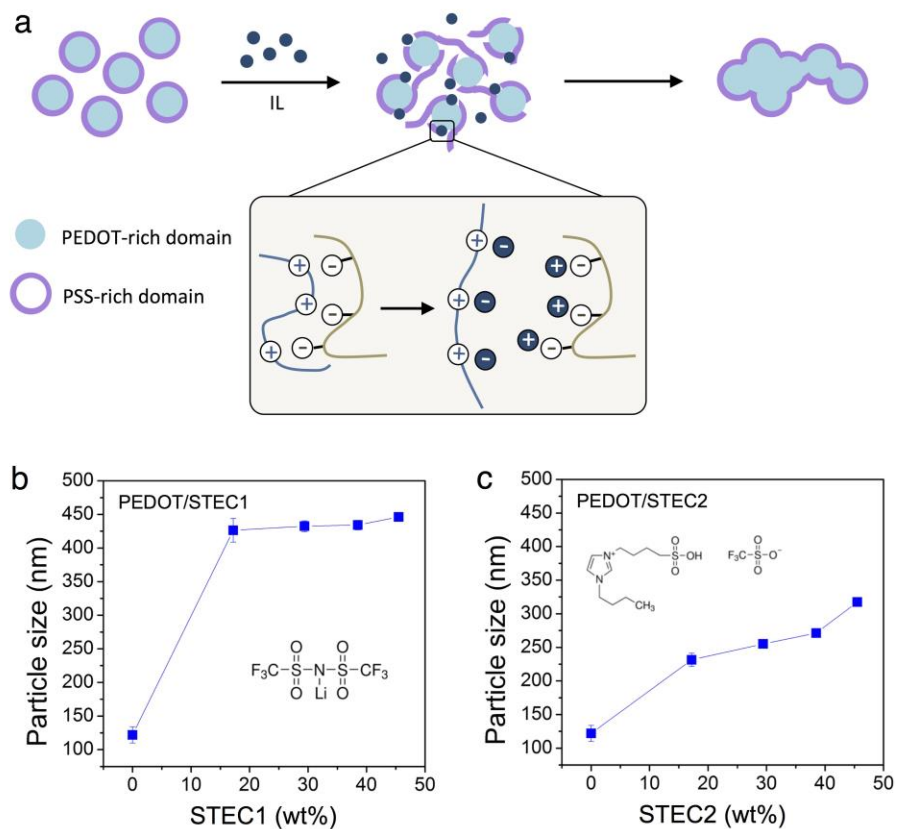


fig. S3. Mechanism behind STEC-induced morphology change for PEDOT:PSS

films. (a) Schematic representation illustrating the effect of STEC on enhancing the phase separation of the PEDOT-rich and PSS-rich domains. (b) and (c) show the average particle sizes in PEDOT:PSS aqueous dispersions with different additive concentrations.

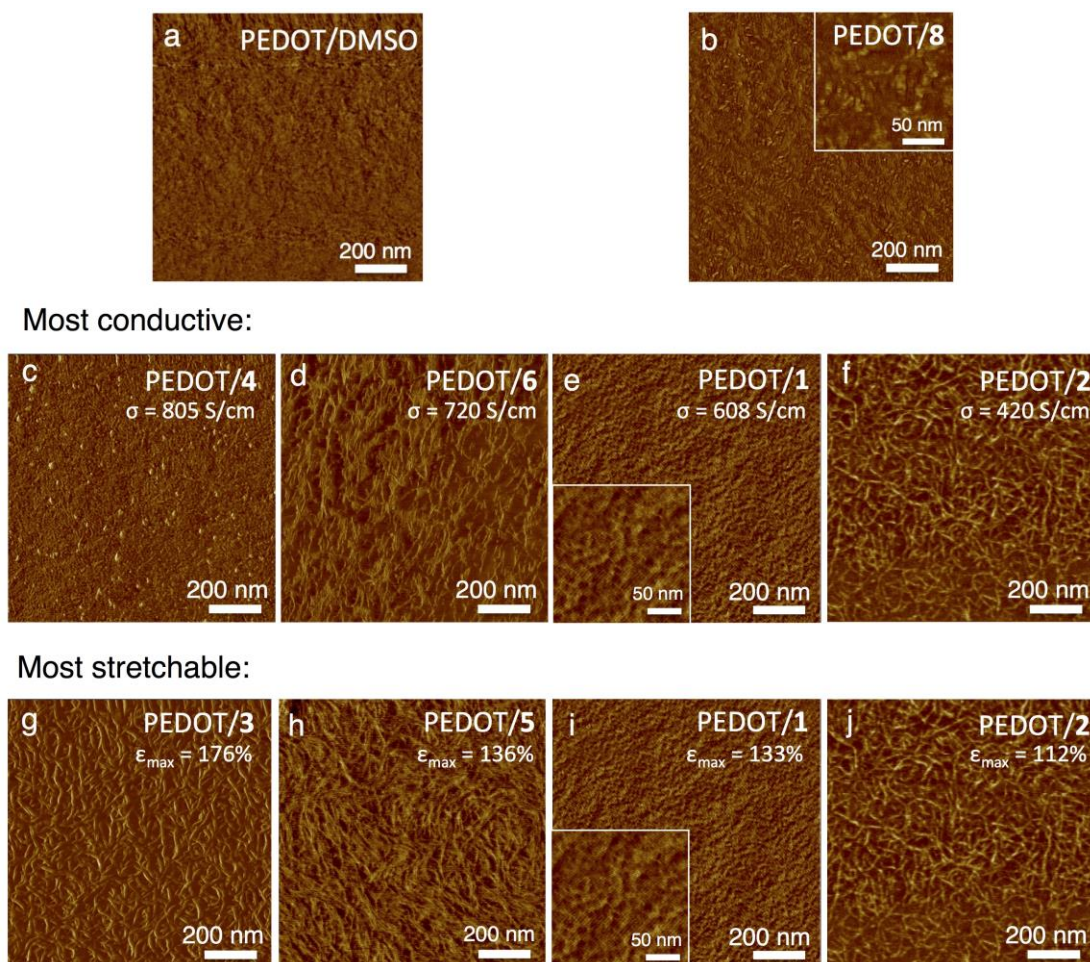


fig. S4. AFM phase images of PEDOT with various additives. (a) shows the morphology of PEDOT without any STEC; (b) shows film with STEC8—an additive that does not enhance stretchability nor conductivity. (c)-(f) are the morphology of the films with the highest conductivity (conductivity marked on each image), and (e)-(h) show those that are the most stretchable (maximum tensile strain labeled on each image). Insets in (e) and (i) are magnified views showing the film features.

(b) Effect on the crystalline regions

As we noted in the previous section, not all STEC additives lead to an enhancement of conductivity despite the clearer phase separation between the PEDOT- and PSS-rich regions. This observation indicates there are other factors at play.

PEDOT:PSS is a semicrystalline polymer, where small PEDOT-rich crystallites are distributed within a disordered matrix. Such structure is reflected by the high background scattering intensity in the GIWAXS patterns (fig. S5, a to e). GIWAXS analysis shows that the PEDOT/STEC with high conductivity, such as PEDOT/STEC1 or 2, exhibit significantly higher crystallinity (fig. S5, d and e) despite being highly stretchable, suggesting the STEC plasticizers are likely distributed in the disordered matrix. The corresponding near out-of-plane intensity plots are shown in fig. S5, f and g. For the PEDOT film without any STEC additives, three peaks were observed along q_z : $q_z = 0.57 \text{ \AA}^{-1}$ ($d = 11.2 \text{ \AA}$), 1.33 \AA^{-1} ($d = 4.9 \text{ \AA}$), and 1.87 \AA^{-1} ($d = 3.4 \text{ \AA}$), which can be indexed as PEDOT (200), PSS amorphous scattering, and PEDOT (010), respectively (*Proc. Natl. Acad. Sci.* 2015, **112**(46): 14138-14143; *Synth. Met.* 2000, **113**(1–2): 93-97). With the addition of STEC, the diffraction peak corresponding to lamella packing, (200), becomes much better defined and increase in relative intensity (fig. S5, d and e). Meanwhile with the addition of ILs, a new peak emerges at $q_z = \sim 0.89 \text{ \AA}^{-1}$ ($d = \sim 6.8 \text{ \AA}$), which was also reported elsewhere in the literature and assigned to PEDOT, but no definitive index was reported. In addition, we observed this peak in the non-soluble PEDOT:PF₆ system (fig. S6), further confirming it arises from PEDOT scattering. The more profound presence of lamella packing peaks indicates the PEDOT/STEC samples have better ordered crystalline domains than that without any STEC additive. Interestingly, the (200) d-spacing increases with increased STEC contents in the films, which is accompanied by a slight decrease in d-spacing for the (010) peak (from 3.4 \AA to 3.3 \AA). This again suggests an increase in the degree of molecular ordering and local crystallinity (*Phys. Rev. Lett.* 2012, **109**(10): 106405). Similar diffraction results have been reported previously in highly conductive PEDOT:PSS obtained by H₂SO₄ treatment (*Adv. Mater.* 2014, **26**(14): 2268-2272; *Adv. Mater.* 2015, **27**(22): 3391-3397).

On the contrary, for the STEC additives (i.e. **5** or **8**) that lead to low conductivities, the GIWAXS patterns more closely resemble the pure PEDOT:PSS films (fig. S5, b and c), without indications of better ordered PEDOT crystalline domains. AFM phase image shows that PEDOT/STEC5 has a well-connected, fibrous structure (fig. S4h) similar to some of the samples that are highly conductive, but its conductivity is orders of magnitude lower (~ 3.4 S/cm) (table S1 and fig. S1). GIWAXS reveals that the PEDOT/STEC5 system is highly disordered, with a weak PEDOT π - π stacking (010) peak along the q_z direction, and a broad PSS scattering ring. The PEDOT (200) peak that is present in pure PEDOT:PSS and PEDOT/STEC1 or 2 films was not even observable. This lack of order in the PEDOT-rich domains is likely to be responsible for the low conductivity as the interchain charge transport is not efficient. Furthermore, PEDOT/STEC8, another system with low conductivity (0.3 S/cm), has a rather similar diffraction pattern as pure PEDOT:PSS (fig. S5c) and doesn't exhibit the $q_z = \sim 0.89 \text{ \AA}^{-1}$ ($d = \sim 6.8 \text{ \AA}$) peak that is associated with PEDOT that has higher crystallinity and conductivity. Hence, a combination of preferred phase separation and high crystallinity of the PEDOT-rich domains are necessary for achieving high conductivity in PEDOT/STEC.

To further confirm the indexing of the PEDOT/STEC systems, we carried out control experiments by collecting GIWAXS patterns of individual STEC, neat PSS blended with 45-70 wt% STEC, and an insoluble PEDOT mechanically grinded with 45-70 wt% STEC (see part (c) and fig. S7 for experimental details). Figure S6 shows the GIWAXS patterns and the corresponding intensity plots for near q_z direction. Neat PSS only showed two broad diffraction rings (fig. S6a), but several diffraction arcs appeared with the addition of STEC2 (fig. S6b). The peak at $q_z = 1.36 \text{ \AA}^{-1}$ matches with the one in the PEDOT:PSS/STEC2 scattering images, further confirming it originates from PSS. For the insoluble PEDOT/PF₆, characteristic scattering peaks similar to that of the PEDOT:PSS/STEC2 was observed (fig. S6, c to e), confirming our interpretation of PEDOT:PSS/STEC2 patterns. The weak diffraction at $q_z = 1.28 \text{ \AA}^{-1}$ is likely from the interactions between PF₆⁻ ions. The crystallinity is largely decreased after the addition of STEC2 (fig. S6, d and e), likely as a result of the plasticizing effect. Note that neat PSS

becomes more crystalline after the addition of STEC2, while insoluble PEDOT:PF₆ less crystalline, which is the opposite trend of the PEDOT:PSS system. The inter-mixing of two charged polymers can readily change the interaction within the individual components, hence have very different effects on the relative crystallinity. Also, neat STEC1 and 2 did not lead to any diffraction patterns, which further indicates that none of the peaks from fig. S5 originates from STEC aggregates.

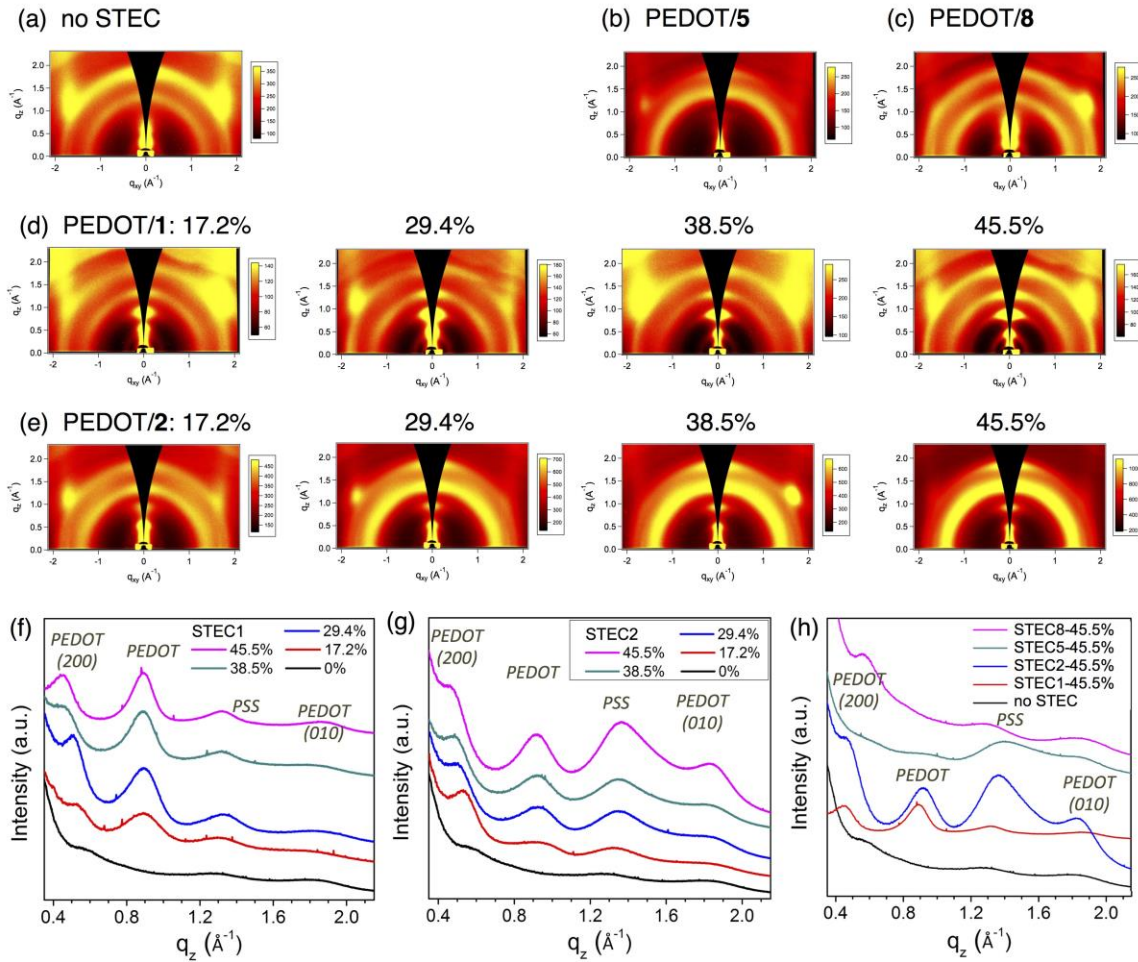


fig. S5. GIWAXS analyses of PEDOT films. GIWAXS 2D images of PEDOT films without any STEC additives (a), with additive (45.5 wt%) that lead to high stretchability but poor conductivity (b), both low stretchability and conductivity (c). GIWAXS patterns of STEC additives that result in a combination of high stretchability and conductivity are shown in (d) and (e). The percentage of STEC in PEDOT:PSS films are indicated on top

of the respective 2D images. (f) and (g) are the line cut plots for the scattering images in (d) and (e), respectively, averaging the scattering intensity within a 30-degree wide sector around vertical q_z direction. (h) combines the line cut plots of PEDOT:PSS films without any STEC additives and those with 45.5 wt% of different additives for comparison.

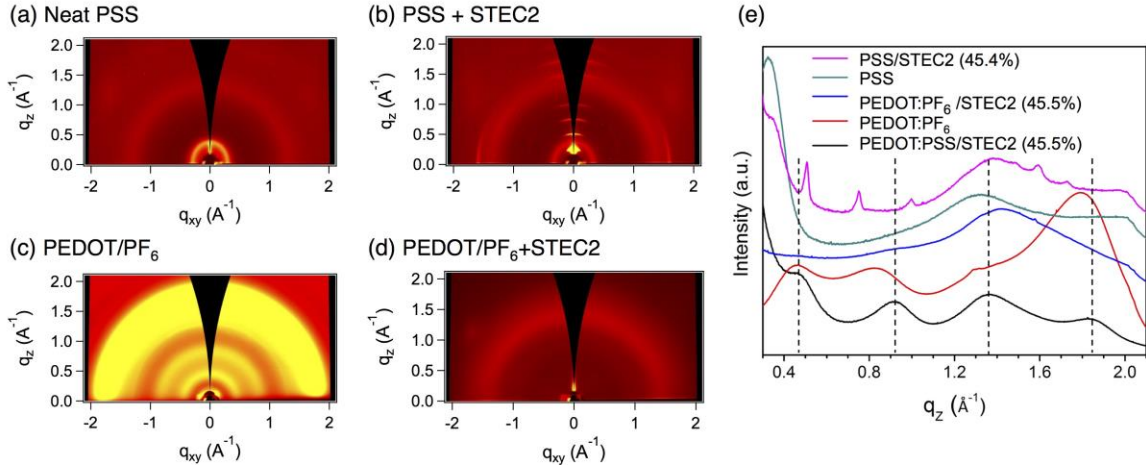


fig. S6. Diffraction data for PSS and insoluble PEDOT control samples. (a)-(d) GIWAXS data for (a) neat PSS (MW $\sim 200,000$ Da), (b) PSS + 45.5 wt% STEC2, (c) PEDOT/PF₆, and (d) PEDOT/PF₆ + 45.5 wt% of STEC2. (e) Line cut plots of (a)-(d) along the q_z direction (30-degree width sector) compared to that of PEDOT:PSS with 45.5 wt% of STEC2.

(c) Effect on mechanical properties

Despite the much-enhanced crystallinity of the PEDOT films with STEC1 or 2 addition, these films also possess higher stretchability. The increase in crystallinity mostly corresponds to the PEDOT-rich domains, which suggests the plasticizers are likely dispersed in the disordered matrix. To probe the interaction between STEC and PEDOT:PSS, we incorporated STEC into PEDOT and NaPSS separately. Insoluble PEDOT:PF₆ was synthesized according to a previous procedure. The product is a black

powdery substance (fig. S7a). Vigorous sonication of this powder in water for 1 h yielded a dark dispersion (fig. S7b, left). However, the particles settled out within minutes, confirming its insoluble nature (fig. S7b, right). When 45.5 wt% of STEC2 was grinded with the PEDOT powder, a homogeneous paste was formed (fig. S7c), while incorporating 62.5 wt% of STEC2 led to a gel-like substance (fig. S7d). Therefore, STEC can serve as an effective plasticizer for the PEDOT component in PEDOT:PSS. Previously, STEC has been shown as an effective medium for dispersing the otherwise insoluble CNTs, which allowed for their homogeneous distribution in an elastic fluoro-polymer as stretchable conductors.⁵ The STEC has a similar effect in dispersing the insoluble PEDOT here. Unfortunately, the paste with 45.5 wt% STEC2 has poor film forming property, likely due to the low molecular weight of PEDOT, hence prohibited it from tensile strain/stress testing.

45.5 wt% of STEC2 was also incorporated into NaPSS. We chose the MW ~200,000 Da grade as it is the closest in molecular weight to the PSS in Clevios PH1000 (400,000 Da) (*Displays* 2013, **34**(5): 423-436). A much lower modulus and a significantly enhanced maximum tensile strain is observed for the NaPSS film with STEC compared to the pristine NaPSS, indicating its plasticizing effectiveness. Therefore, due to the strong interaction between STEC and both PEDOT and PSS components, we propose that STEC plasticizers are incorporated in the disordered domains of PEDOT:PSS, rendering the films highly stretchable.

Furthermore, it has been proposed that the fibrous network formed from phase separation between PEDOT and PSS are crucial for achieving stretchability (*Adv. Funct. Mater.* 2015, **25**(3): 427-436). We observe that the PEDOT/STEC films with the highest stretchability all possess some level of fibrous or web-like morphology (fig. S4, g to j). However, morphology alone does not guarantee high stretchability; for instance, PEDOT/STEC6 (fig. S4d) also exhibit well-defined fibrous morphology, but is only moderately stretchable (maximum tensile strain = 71% as a free-standing film). Therefore, we propose that it is the combination of the effectiveness of individual STEC

enhancers with the fibrous morphology that results in high stretchability observed in select PEDOT/STEC systems.

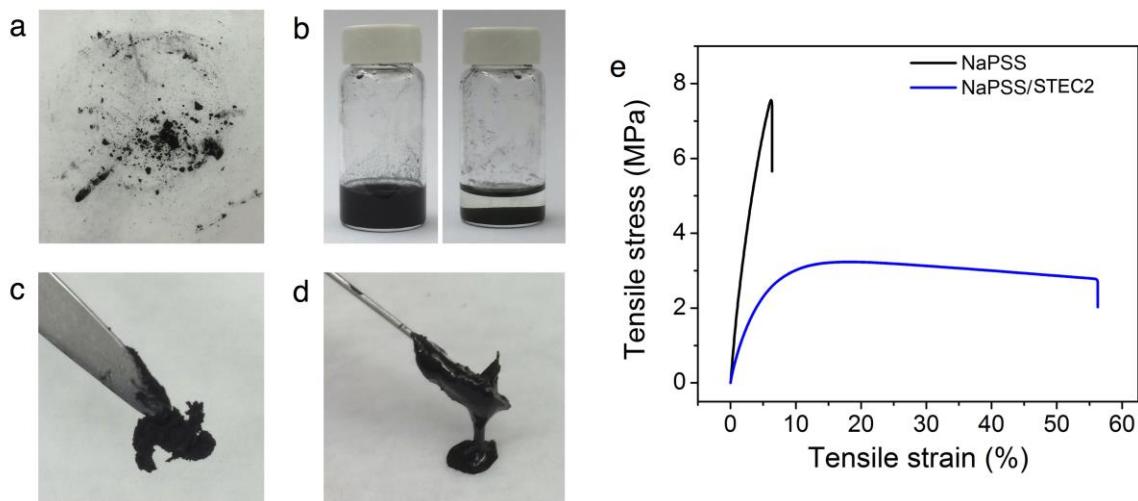


fig. S7. Plasticizing effect of STEC on PEDOT and NaPSS individually. (a) Picture of insoluble PEDOT:PF₆ powder. After sonicating the powder in water for 1 h, an apparently homogeneous dispersion is formed (b, left). However, the particles precipitate out within minutes (b, right), illustrating its insoluble, non-dispersible nature. STEC2 was added to this powder and thoroughly mixed using a mortar and pestle. Picture in (c) shows the paste that was formed after dispersing this PEDOT with 45.5 wt% STEC2, and (d) shows the gel-like substance with 62.5% STEC2 addition. These results illustrate that the STEC can effectively disperse the insoluble PEDOT and have a plasticizing effect. Similarly, 45.5 wt% of STEC2 was added to polystyrenesulfonate sodium (NaPSS) with a molecular weight of 200,000 Da. This molecular weight is chosen as it is the commercially available grade with the closest molecular weight match to those in the PEDOT:PSS (400,000 Da). (e) shows the stress/strain curves of the pure NaPSS films and after the addition of STEC. A much enhanced maximum tensile strain is achieved, which illustrate that STEC has a plasticizing effect for both the PEDOT and the PSS phase.

section S4. Morphology of PEDOT/STEC film interior

SEM analyses show that the PEDOT/STEC2 films have a solid and densely packed cross-section despite the high STEC percentage, indicating the STEC is well dispersed in the polymer network.

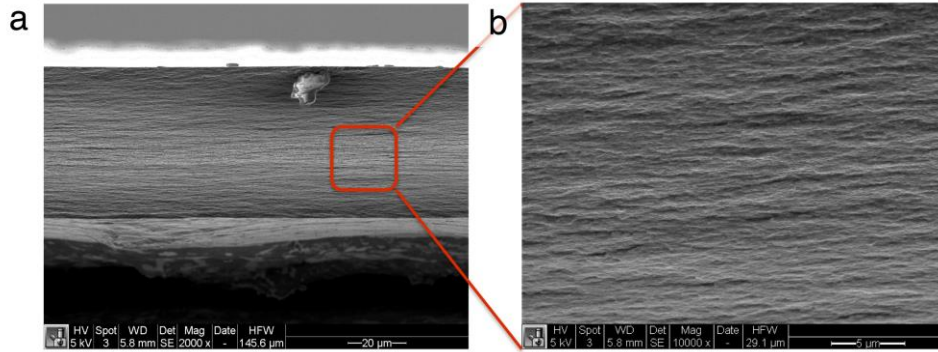


fig. S8. SEM characterization of the cross section of a stretchable PEDOT film. (a) SEM image showing the solid cross-section of a PEDOT film with 45.5% STEC2; (b) offers a zoomed view of (a).

section S5. Microscopy study of the effect of tensile strain on PEDOT/STEC films.

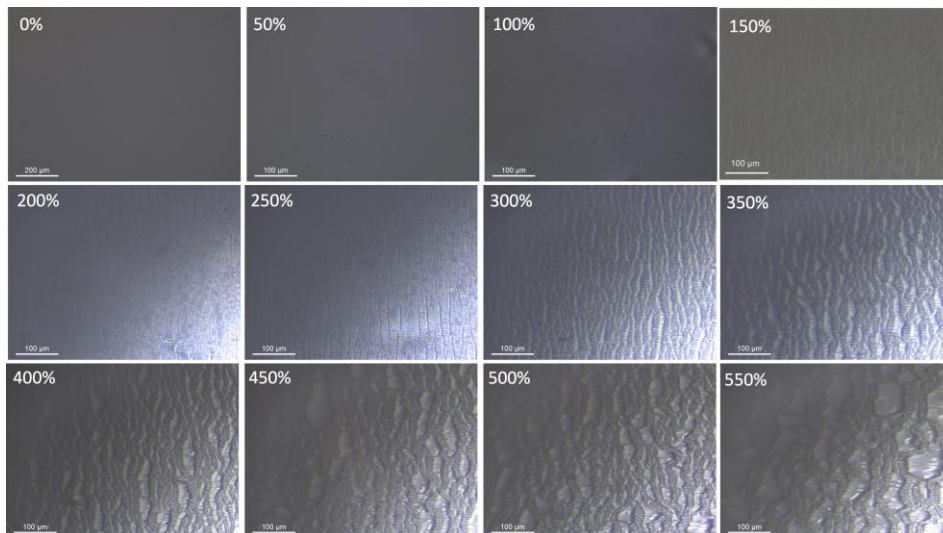


fig. S9. Optical microscope images of a PEDOT/STEC1 film supported on a SEBS substrate under various strains.

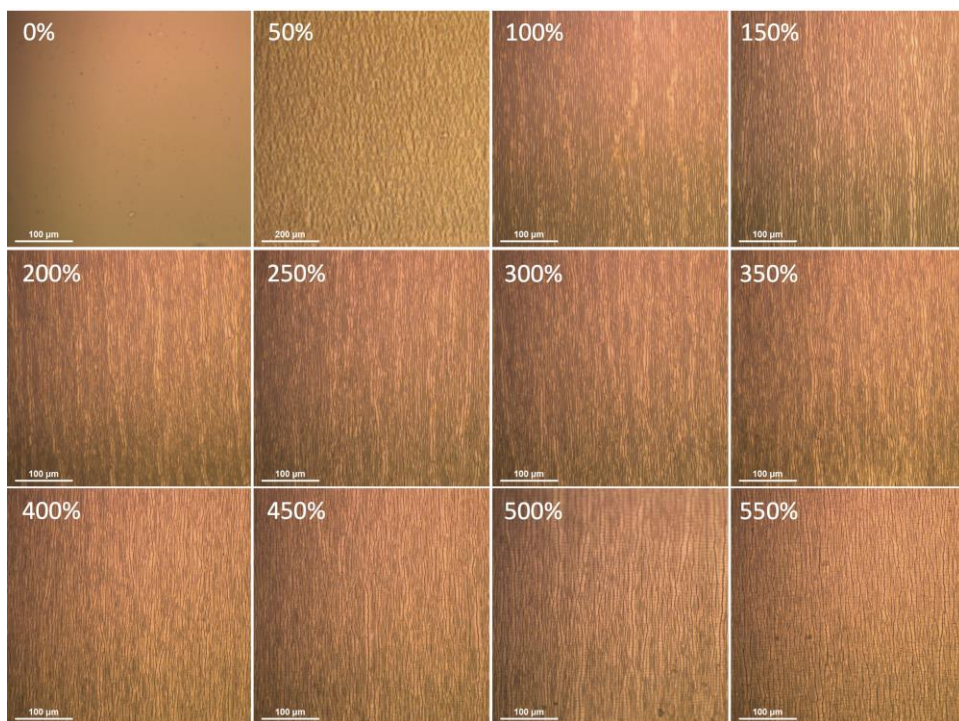


fig. S10. Optical microscope images of a PEDOT/STEC1 film supported on a SEBS substrate after being stretched to various strains and returned to its original length. Folds are formed in the film after stretching as seen from AFM in fig. S11.

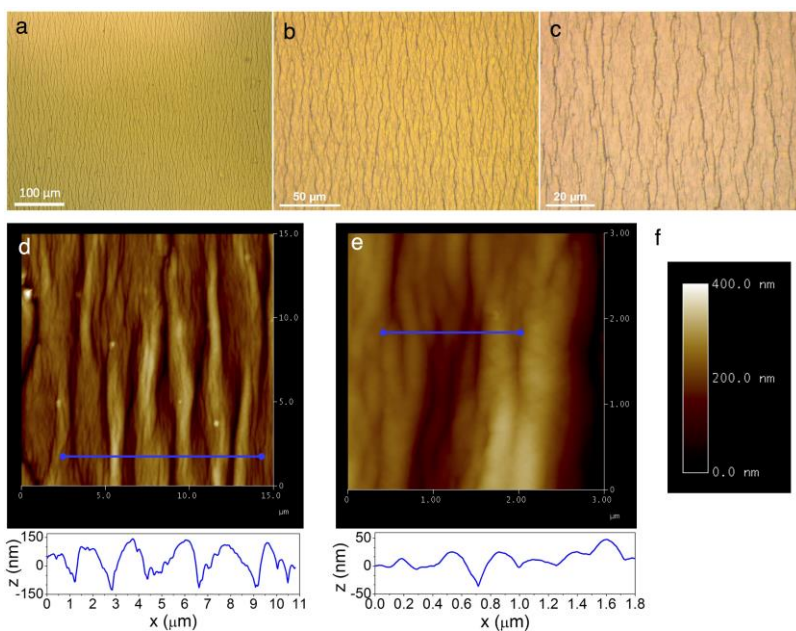


fig. S11. Surface profile analyses of PEDOT films after stretching. (a)-(c) Optical Microscope images at various magnifications showing a PEDOT/STEC1 film at 0% strain after cycling 1000 times to 100% strain. (d) and (e) are the corresponding AFM images showing folds in the film.

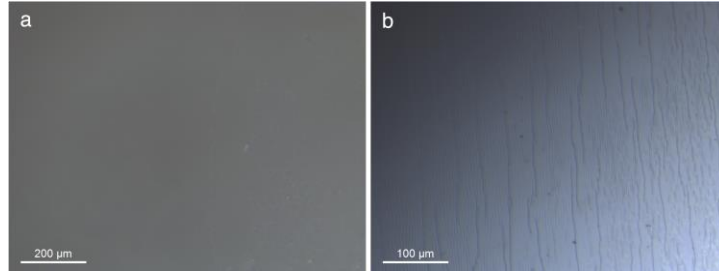


fig. S12. Optical microscope images of a PEDOT/STEC1 film upon unloading from 100% strain. (a) At 80% strain, (b) at 70% strain where wrinkles are seen, indicating the onset of plastic deformation.

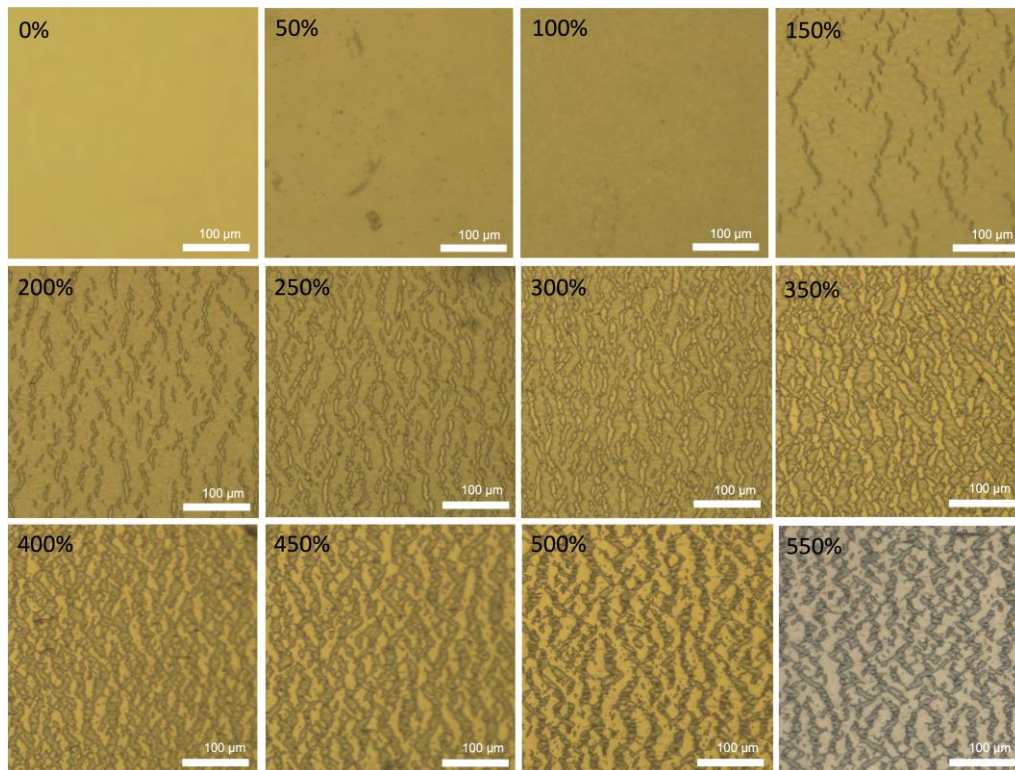
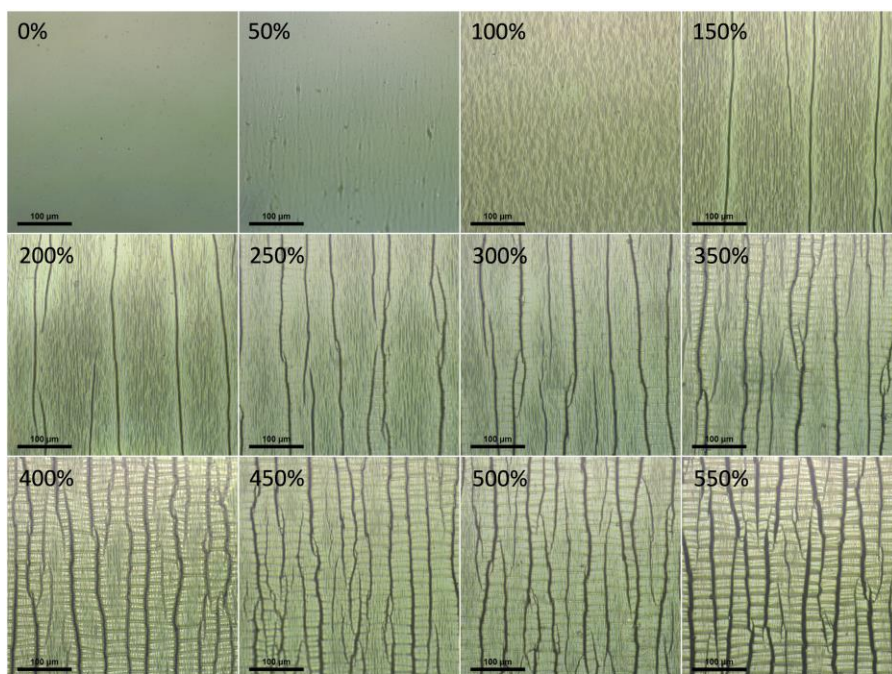


fig. S13. Optical microscope images of a PEDOT/STEC2 film held under various tensile strains.



PEDOT/ILASTE2, 100%, 1000 cycles

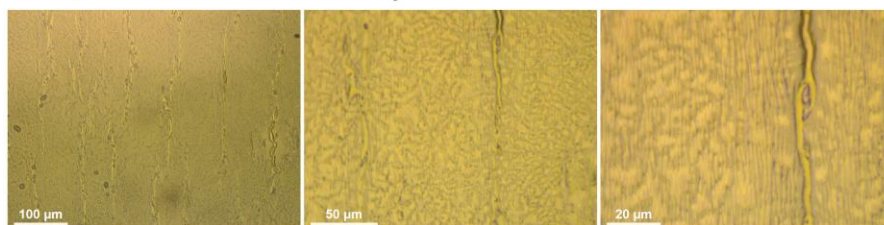


fig. S14. Optical microscope images of a PEDOT/STEC2 film upon stretching to various tensile strains. Optical microscope images of a PEDOT/STEC2 film after being stretched to the indicated percentage (top panel); optical microscope images at various magnifications of a PEDOT/STEC2 film after being cycled 1000 times to 100% are shown in the bottom panel. The rippled pattern visible on the film after 100% strain are folds, whereas the dark vertical lines that appear beyond 150% are cracks.

section S6. Electrical properties of PEDOT/STEC films

(a) Conductivity of as-processed vs. treated films

Conductivity is largely influenced by the processing method of PEDOT/STEC due to the different drying kinetics that can lead to different film morphology and chain arrangement. Values for drop cast thick films (>20 μm) and spin coated thin films containing various STEC contents are presented below. We found that an additional STEC solution soaking process can further enhance the conductivity. In this process, we drop a 10 mg/mL STEC aqueous solution on top of an annealed PEDOT film, wait for 60-90 seconds, then remove the excess solution with a fast spin speed (3000 rpm). The resulting films exhibit a higher PEDOT content on the surface (see fig. S17 and corresponding text for detailed discussion) and an enhanced conductivity (figs. S15c, and S16).

For PEDOT/STEC1-3 samples, which are model systems in our study, a rapid increase in conductivity was observed as the STEC concentration increased until ~45 wt% (Fig. 4a). The highest conductivity values achieved were 2588, 3102, 2544 S/cm at 71 wt% STEC1, 2, 3, respectively. This great enhancement in conductivity compared to the original PEDOT:PSS is at least partly attributed to the doping and chain straightening effects resulted from STEC-induced charge screening. For STEC1 and 2, due to the strongly electron-withdrawing CF_3 moieties, the anions have much higher acidity than the PSS anions, which render them effective dopants for PEDOT in addition to serving as plasticizers and tuning microscopic morphology. The anion in STEC3 has a similar acidity as PSS; therefore, a much slower increase in conductivity was observed with the increase of STEC content. At high STEC3 concentration, a similarly high conductivity was achieved, possibly due to the abundance of STEC anions, which are more effective dopants than the polymeric PSS due to their greater mobility between polymer chains, as previously observed for tosylate anions. PEDOT with other STEC additives show similar behavior, which are illustrated in figs. S15 and S16.

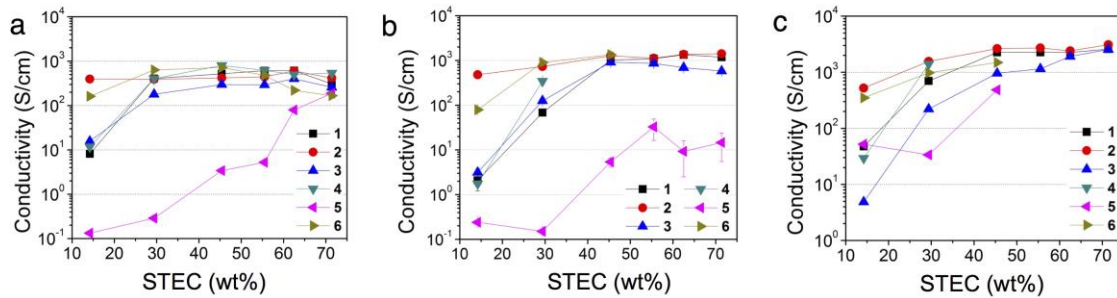


fig. S15. Conductivity values of PEDOT/STEC films processed under different conditions. Conductivity of PEDOT/STEC films in relation to the ionic liquid additive contents prepared by **(a)** drop casting (thick films of 20-200 μm), **(b)** spin coating (thin films of 50-200 nm), and **(c)** spin coating then further treated with the corresponding STEC aqueous solution.

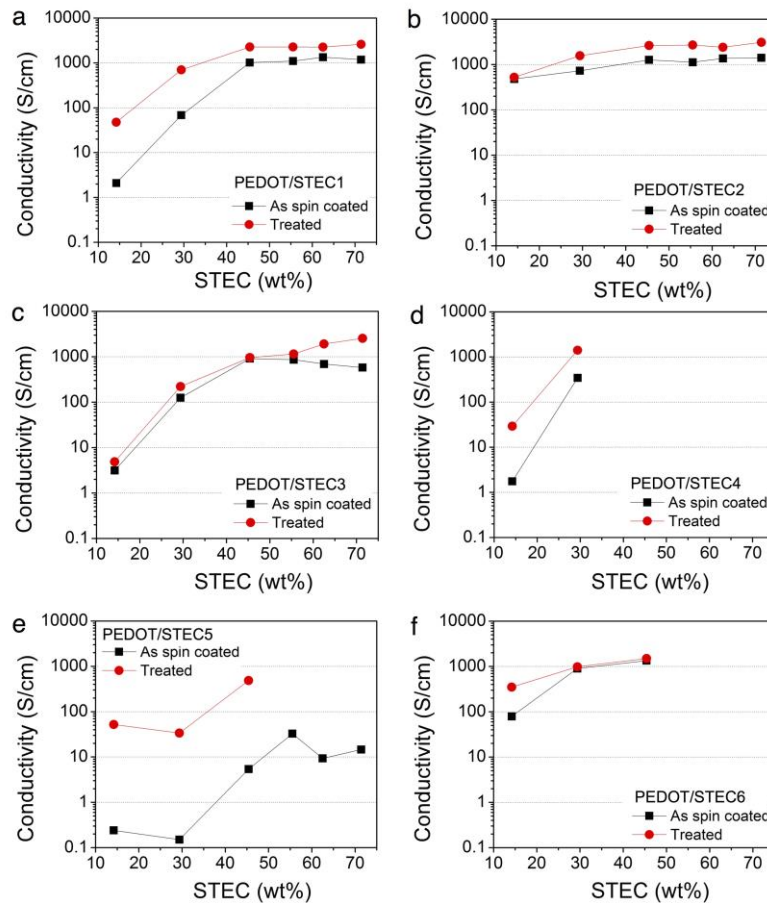


fig. S16. Conductivity of PEDOT/STEC films with various STEC weight % before and after further STEC solution treatment. (a)-(f) represents PEDOT with STEC1-6, respectively. For PEDOT with STEC4 (d) and 6 (f), the dispersion quickly gels up on mixing with higher STEC content, which results in highly inhomogeneous, non-continuous films. Therefore, the conductivity values were not measured. For PEDOT films with high STEC5 content, the films get partially delaminated after the soaking step, rendering conductivity measurement difficult; hence values not shown.

(b) Chemical characterization of solvent-treated films

To understand the additional STEC aqueous solution treatment step on stretchable PEDOT, we carried out XPS and AFM studies. The film thickness decreases for all films

after the STEC solution soaking regardless of the STEC used (fig. S17a). XPS of the film surface reveals that a higher PEDOT content is exposed (peak ~ 163 - 165 eV) and the PSS+STEC amount (~ 168 - 170 eV) decreases (fig. S17b). Similar observations can be seen from the AFM images in fig. S17, c to f, as the PEDOT phase content is visibly higher, as indicated by the more fiber-like structures. Control experiments of dropping water instead of STEC solution on top of the annealed PEDOT films lead to a similar decrease in thickness and increase in conductivity. We used STEC aqueous solutions here in order to wash away PSS but minimize STEC loss as they serve as plasticizers.

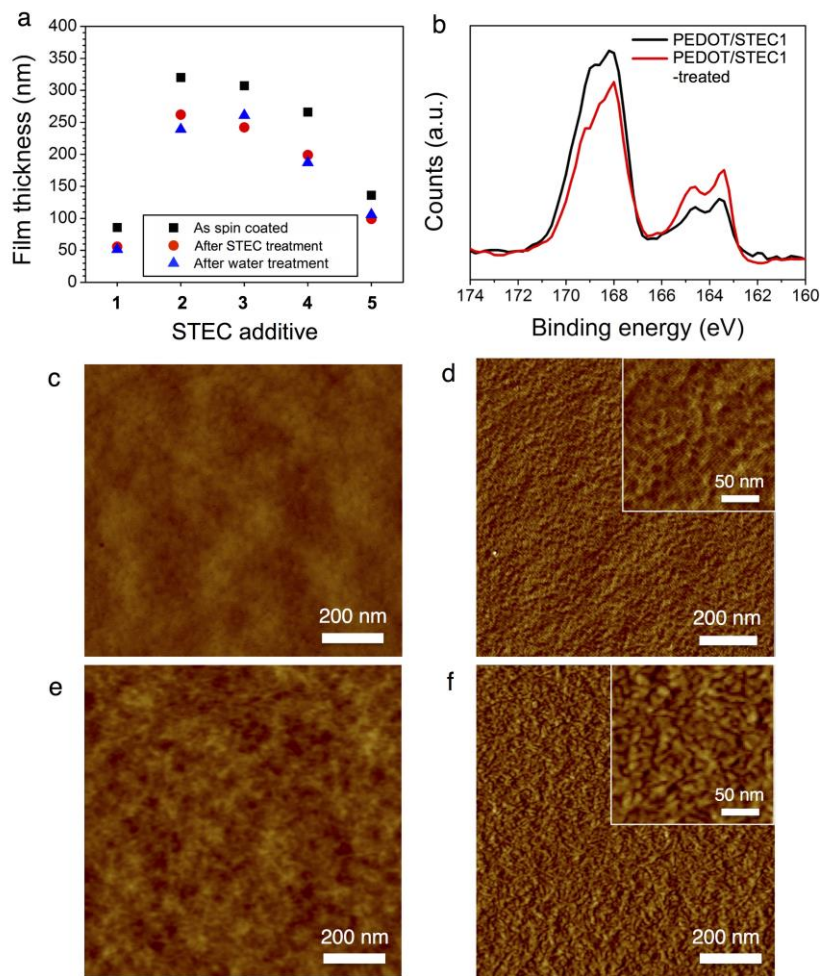


fig. S17. Effect of further doping using STEC solution on spin-coated films. (a) Change in film thickness (STEC content = 45.5%); (b) XPS spectra comparing the change in chemical composition; (c) height and (d) phase AFM images of a

PEDOT/STEC1 film obtained by spin coating; (e) height and (f) phase AFM images of the same film after further doping with STEC solution.

section S7. Composition of PEDOT/STEC films

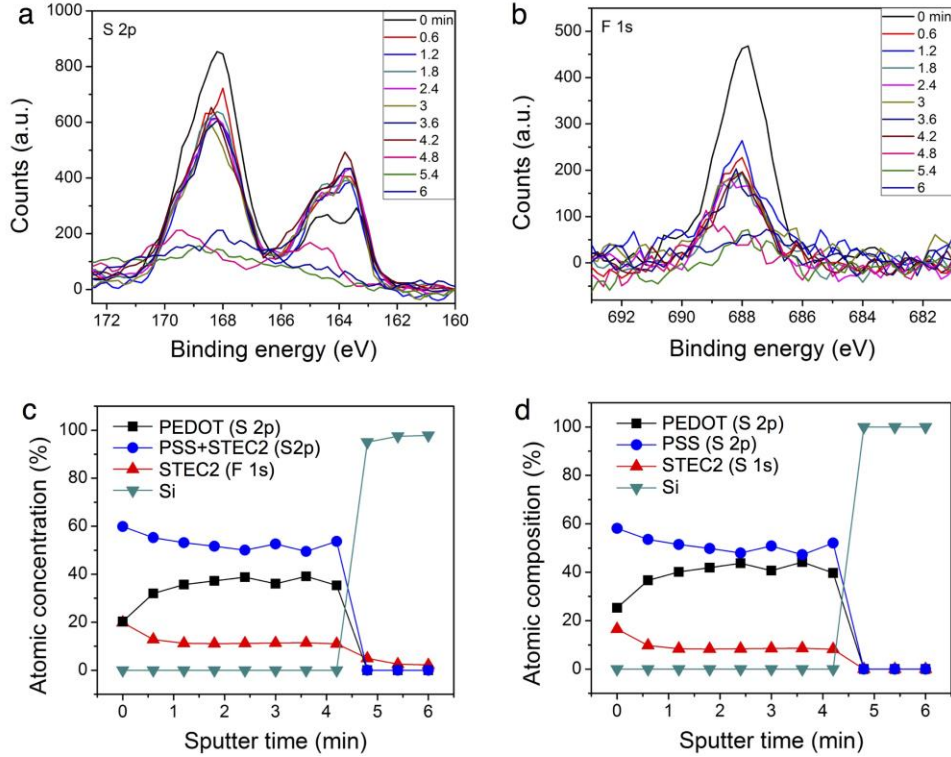


fig. S18. Chemical composition of PEDOT/STEC films. (a)-(b) XPS spectra of a PEDOT/STEC2 film with various C_{60} ion gun sputtering duration for S 2p (a) and F 1s (b). (c) Atomic ratio between the integrated S 2p and F 1s peaks showing the relative ratios of the various elements in the film. (d) Relative composition of PEDOT, PSS, and STEC2 along at various depths. The composition of STEC2 (S 2p) is determined by the stoichiometric conversion of the F 1s peak based on the molecular structure. PSS (S 2p) composition can thus be obtained by subtracting the STEC2 (S 2p) percentage from the PSS+STEC2 (S 2p) values in (c).

section S8. Low-temperature measurements

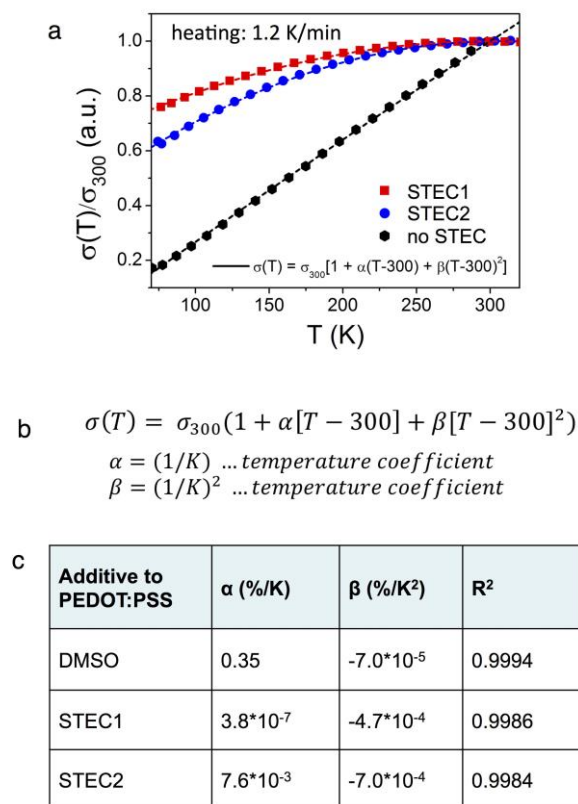


fig. S19. Temperature-dependent conductivity and first- and second-order temperature coefficients for PEDOT films. (a) Temperature-dependent conductivity of PEDOT films with various additives; (b) equation for extracting temperature coefficients; (c) Table showing the first and second order temperature coefficients of the films.

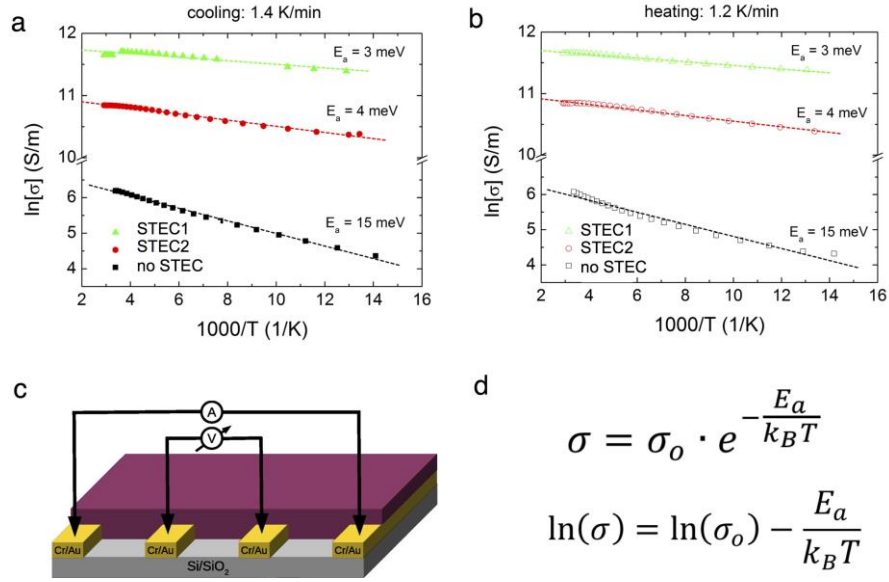


fig. S20. Arrhenius plots for temperature dependent conductivity. Arrhenius plots for PEDOT with various additives upon (a) cooling and (b) heating; (c) schematic illustrating the measurement geometry; (d) equations for extracting activation energy from the temperature dependent conductivity behavior.

section S9. FoM for transparent conductors

A key standard for evaluating a transparent conductor is its figure of merit (FoM), which is defined as the ratio of its direct current conductivity (σ_{dc}) to optical conductivity (σ_{op}):

$$FoM = \frac{\sigma_{dc}}{\sigma_{op}(\lambda)} = \frac{188.5 \Omega}{R_{sh} \cdot (T(\lambda)^{-\frac{1}{2}} - 1)},$$

where R_{sh} is the sheet resistance, T is the optical transparency at a specified wavelength λ (550 nm). A FoM of 35 is typically the required benchmark value for a transparent conductor to be commercially viable (*Adv. Funct. Mater.* 2011, **21**(6): 1076-1081). Our stretchable PEDOT/STEC exhibit FoM above 100 for all thicknesses tested (Fig. 4e), with a value as high as 142 for the film with 96% transmittance. It surpasses the previous highest value from spin-casted PEDOT films (i.e. FoM = 72 for H_2SO_4 -treated films).

section S10. Testing geometry for PEDOT films under tensile strain

A dumbbell geometry is used for the resistance vs. strain experiments to promote uniform deformation within the stretched region (fig. S21a). Four parallel EGaIn electrodes were deposited either in parallel or perpendicular to the stretching direction to probe anisotropic conductivity (fig. S21b). The dimension change between the electrodes was measured at each strain value and the film thickness change was extracted using optical measurements. Conductivity values were then calculated using the equation in fig. S21c.

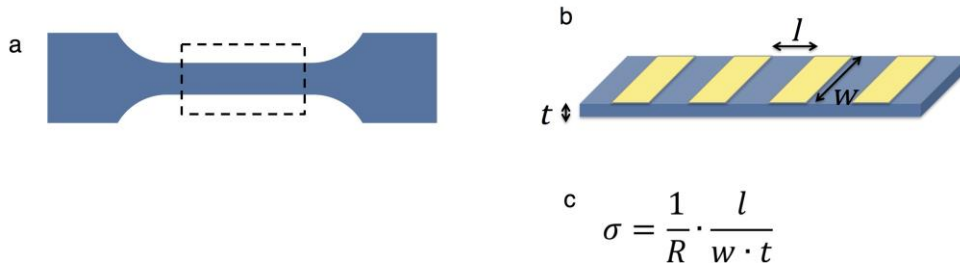


fig. S21. Schematic diagrams of tensile testing and conductivity measurement geometries. (a) Geometry of PEDOT films used for testing resistance change under tensile strain. The dashed rectangle represents area being stretched. (b) Four-point probe measurement geometry and (c) equation for calculating conductivity.

section S11. Polarized UV-vis-NIR spectra for PEDOT films under tensile strain

To study the anisotropy in PEDOT/STEC films upon stretching, polarized UV-vis-NIR spectra were collected. fig. S22a shows the unpolarized spectra for the PEDOT/STEC1 film under various strains. The absorbance consistently decreases with increasing strain because the film is getting thinner. However, the peak around 810 nm becomes more pronounced with increasing strain, and two small peaks around 570 and 620 nm appear. These peaks are all associated with dedoped PEDOT, indicating some level of dopant removal of the film as the strain is increased. However, when the incident light is polarized parallel to the stretching direction, the intensity of the free-carrier tail that extends into the NIR (a bipolaron subgap state) increases in intensity under 0%-125% strain despite the decreasing film thickness, indicating significant amount of chain alignment along the stretching direction (fig. S22b). The peaks associated with dedoping of PEDOT (570, 620 and 810 nm) are also present in these spectra, but not in those with light polarized perpendicular to the stretching direction (fig. S22c). This suggests that as the PEDOT chains are becoming highly aligned, a certain amount of STEC are squeezed out as a result of the tighter interchain packing. XPS analysis (incident beam normal to sample surface) further confirms this behavior as the XPS spectra on F 1s peaks (elements only present in the STEC) show a noticeable increase in relative intensity when the film is stretched to 100% (fig. S23). The ratio between the S 2p peaks associated with PSS+STEC (~172-175 eV) to that of PEDOT (~164-165 eV) increases upon 100% tensile strain too, further indicating the increase in surface STEC content that are squeezed out due to chain alignment. Note that despite this strain-induced dedoping phenomenon, the conductivity of the film increases significantly from 0% to 100% strain along the stretching direction (see Fig. 2a and b and analysis in main text), likely due to the much more efficient carrier transport through the oriented chains. The surface STEC content decreases after the film is relaxed from 100% strain back to 0% (fig. S23), indicating the STEC molecules are partially absorbed back into the film during the process. After 1000 stretching cycles, the surface STEC content becomes almost identical as the pristine film, suggesting an equilibrium is reached after repeated cycling. This cycling-induced equilibrium can also be observed in the dichroic ratio plot in Fig. 2g.

During the first stretch, the PEDOT film has a dichroic ratio of 1 at 0% strain and ~ 2.8 at 100% strain. However, after 1000 cycles to 100% strain, the dichroic ratio of the same film stabilizes at ~ 1.8 at both 0% and 100% strain, indicating equilibrium has been reached.

When UV-vis-NIR is collected with light polarized perpendicular to the stretching direction, a consistent decrease in intensity is observed as opposed to the increase in intensity of the spectra with light polarized in parallel direction, despite the decrease in film thickness due to elongation (fig. S22, b and c). This phenomenon is also likely a result of chain alignment, as the optical density will increase along the stretching direction, but decrease in the perpendicular direction.

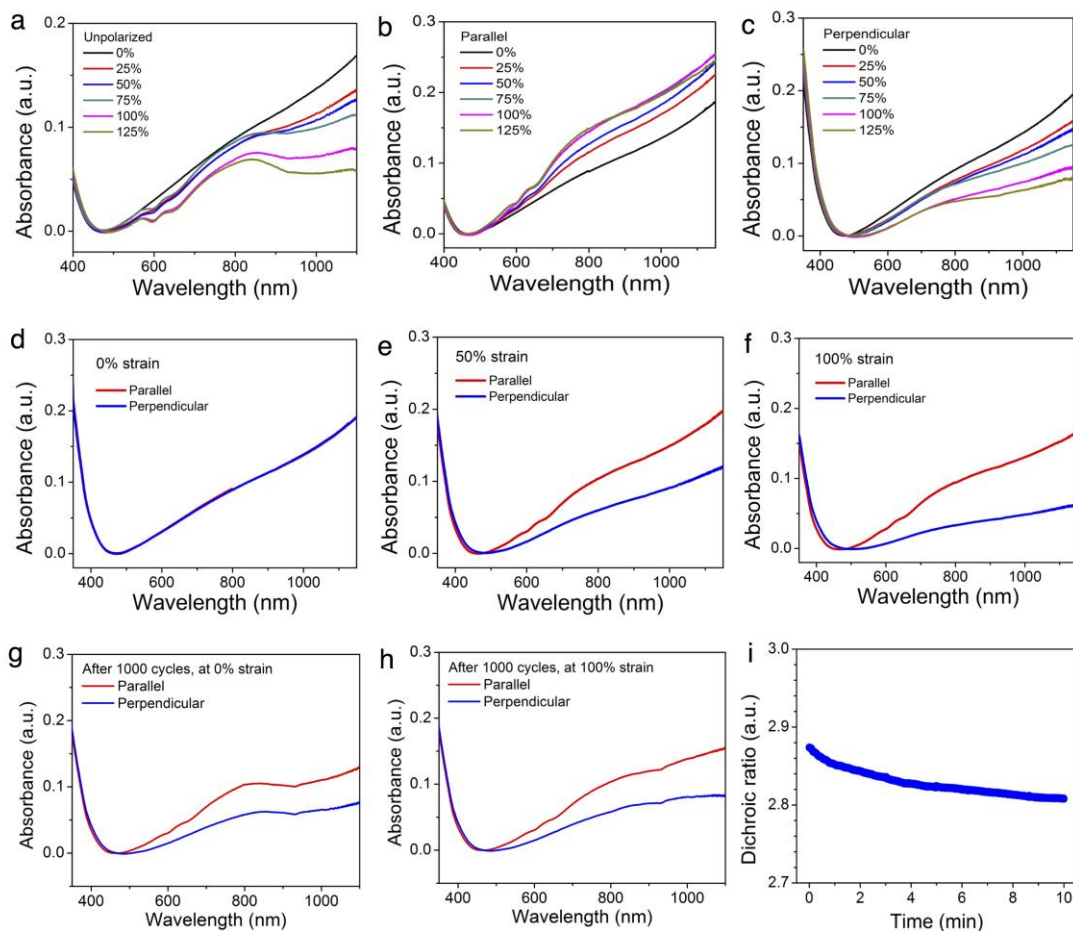


fig. S22. Tension-induced chain-alignment behavior of PEDOT/STEC films. (a) Unpolarized UV-vis-NIR spectra of PEDOT/STEC1 film under various tensile strains. (b) and (c) UV-vis-NIR spectra of the film under various strains measured using incident light that is polarized (b) parallel and (c) perpendicular with respect to the stretching direction; (d)-(f) offer comparison of the polarized UV-vis-NIR spectra along the parallel and perpendicular directions for PEDOT films under 0%, 50%, and 100% strains, respectively. The polarized UV-vis-NIR spectra of a PEDOT/STEC1 film after returning from 1000 cycles to 100% is shown in (g), and those for the cycled film held under 100% strain is shown in (h). (i) The dichroic ratio of the film is monitored over time, which shows a slow decay under constant tension at 100%.

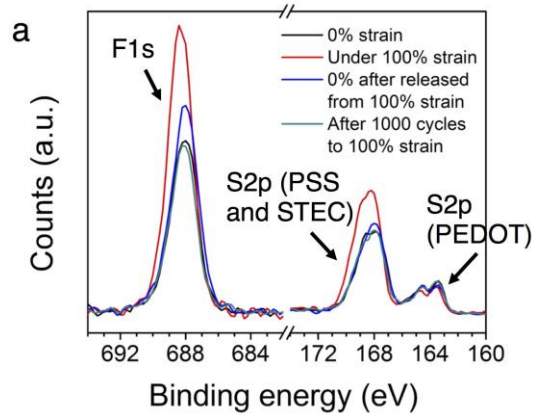


fig. S23. XPS analysis of film surfaces under 0% versus 100% strain, after returning from 100% to 0% strain, and after 1000 stretching cycles to 100% strain.

section S12. Cycling stability and morphological change of PEDOT with STEC additives

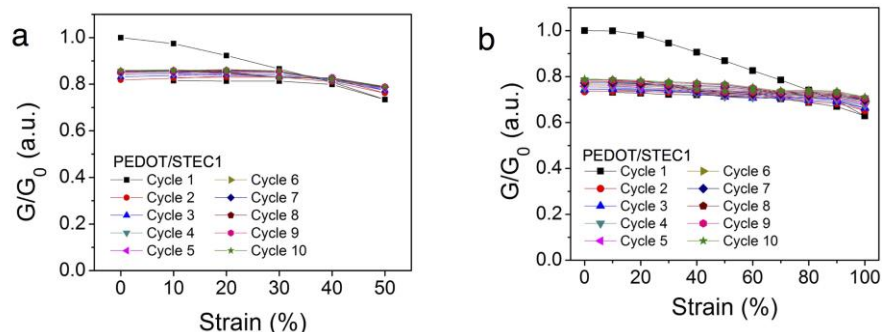


fig. S24. Cycling stability of PEDOT/STEC1 films. Change in PEDOT/STEC1 film conductance under various strains for the first 10 cycles between (a) 0 to 50% strain and (b) 0 to 100% strain. Cycling stability plots are shown in Fig. 2c and d.

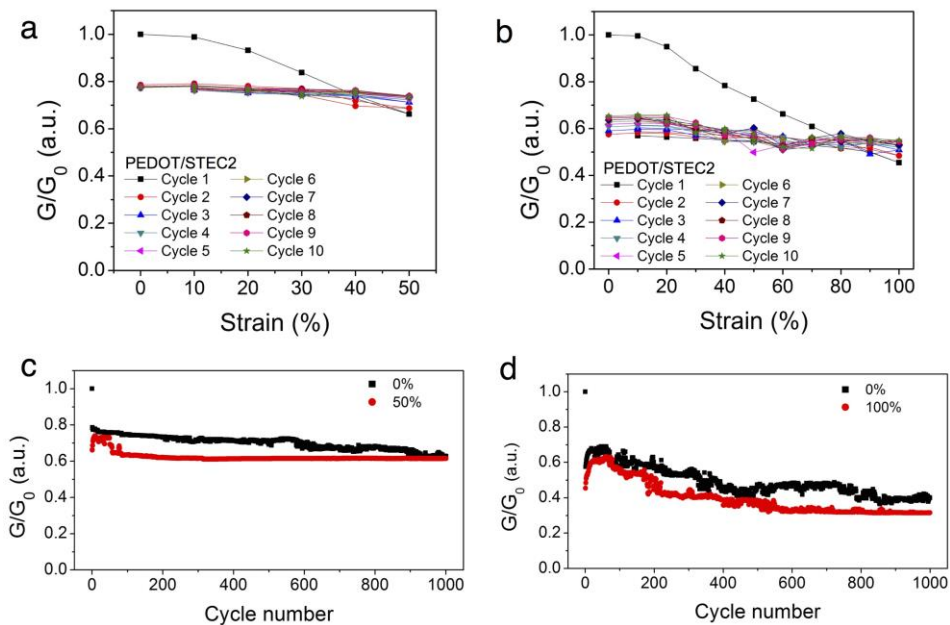


fig. S25. Cycling stability of PEDOT/STEC2 films. Change in PEDOT/STEC2 film conductance under various strains for the first 10 cycles between (a) 0 to 50% strain and (b) 0 to 100% strain. (c) and (d) shows the conductance stability of the films when cycled 1000 times to (c) 50% and (d) 100%.

section S13. Mixed ion-electron conductivity

Figure S26, a and b show the typical electrochemical impedance spectra of PEDOT:PSS with STEC1 in the form of Nyquist plot and bode plot, respectively. The Nyquist plot of PEDOT:PSS with STEC2 shows an inductive line suggesting that it is almost a pure electronic conductor. The inductive line in fig. S26a and small decrease of resistance in high frequency region in fig. S26b are mainly due to the instrumental error. The result shows that PEDOT:PSS with STEC1 samples (n=3) have resistance of $4.55 \pm 0.04 \Omega$ under ambient conditions (moisture level ~42%).

Figure S26, c and d show the typical electrochemical impedance spectra of PEDOT:PSS with STEC2 in the form of Nyquist plot and bode plot, respectively. Unlike the PEDOT:PSS with STEC2 sample, the one semicircle in fig. S26c suggests that PEDOT:PSS with STEC2 is a mixed electronic/ionic conductive material. The equivalent circuit of this mixed conductor can be simplified as a parallel combination of electronic resistance, R_e , and ionic resistance, R_i , which is in serial with a capacitor. Then, the intersection of the high frequency line with the real (Z') axis is the resistance of the electronic and ionic resistance in parallel, $R_i R_e / (R_i + R_e)$, and the intersection of the low-frequency line with the Z' axis is the electronic resistance, R_e (*Electrochem. Solid-State Lett.* 2007, **10**(3): A65-A69). The result shows that PEDOT:PSS with STEC1 samples (n=3) possess electronic resistance of $51.5 \pm 9.2 \Omega$ and ionic resistance of $68.1 \pm 12.7 \Omega$ under ambient conditions (moisture level ~42%).

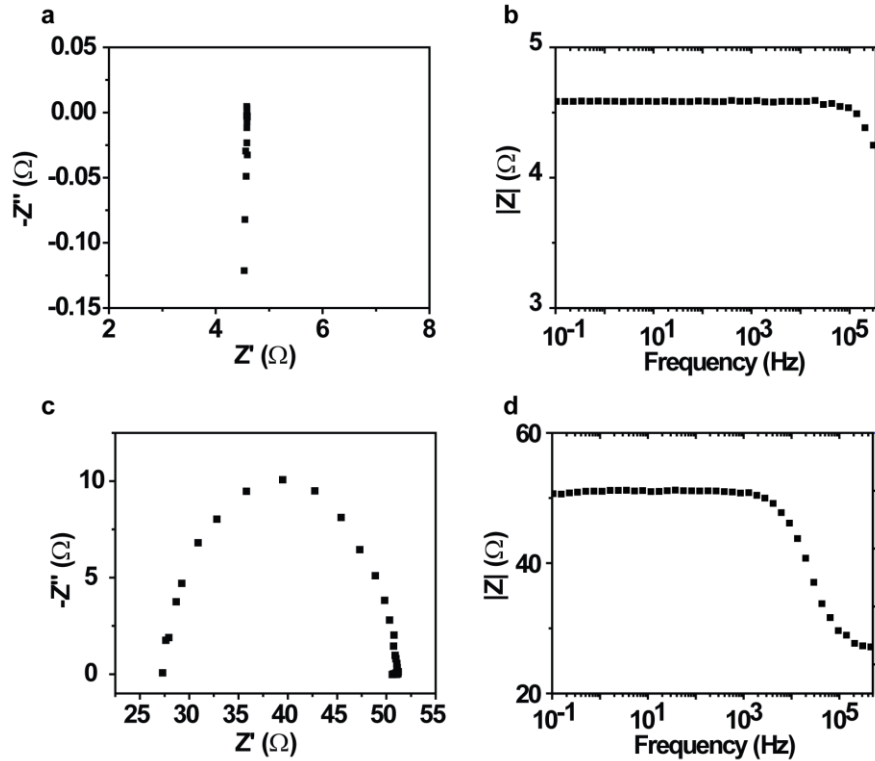


fig. S26. Mixed ion-electron conductivity measurements. (a) Electrochemical impedance spectra of PEDOT:PSS with STEC1 in the form of Nyquist plot. (b) The variation of the impedance of the PEDOT:PSS with STEC1 to the frequency. (c) Electrochemical impedance spectra of PEDOT:PSS with STEC2 in the form of Nyquist plot. (d) The variation of the impedance of the PEDOT:PSS with STEC2 to the frequency.

section S14. PEDOT/STEC as interconnects for FET arrays

The PEDOT/STEC is used as the stretchable interconnect for FET arrays based on rigid-island structures. As the device density increases (i.e. the ratio of the length of a rigid island to that of a PEDOT interconnect increases), the actual strain in the PEDOT interconnects increases monotonically for the same external strain on the entire array. Figure S27 and Fig. 5D illustrate and summarize such effects through finite element simulation. For 2 dimensional arrays (e.g. 3×3), the array was clamped between 2 fitted hollow rings (see Supplementary video 3 for setup) to enable uniform stretching in all

directions. Schematic and calculations for areal strain is shown in fig. S28b. The FET transfer characteristics are summarized in figs. S29 to S31 for the a high density (5:1 rigid island:interconnect ratio) one-dimensional array under unidirectional stretching, 3×3 two-dimensional array under multi-dimensional stretching on a flat surface, and an identical 3×3 array under multi-dimensional stretching on a curved surface, respectively. Table S2 summarizes the mobility and threshold voltage shift at 0% and 125% strain for the devices show in fig. S30.

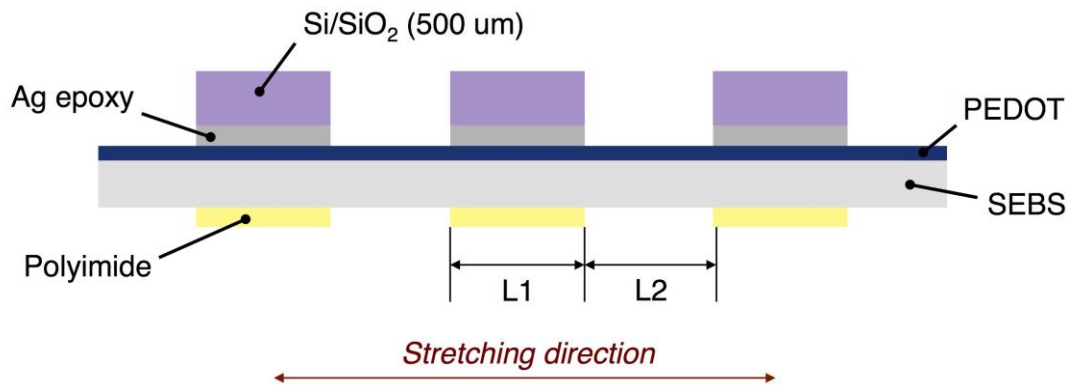
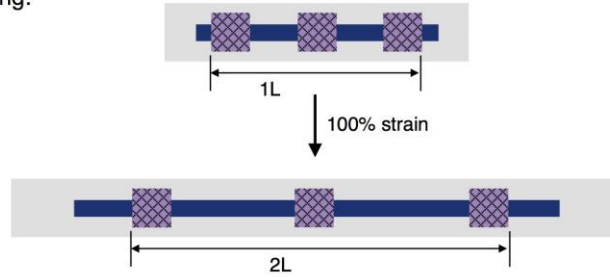


fig. S27. Schematic showing the cross-sectional view of a linear rigid-island array connected with stretchable PEDOT. Schematic showing the cross-sectional view of a linear rigid-island array connected with stretchable PEDOT. It is used for the finite element simulation shown in Fig. 5D.

(a) 1-D stretching:



(b) Multi-dimensional stretching:

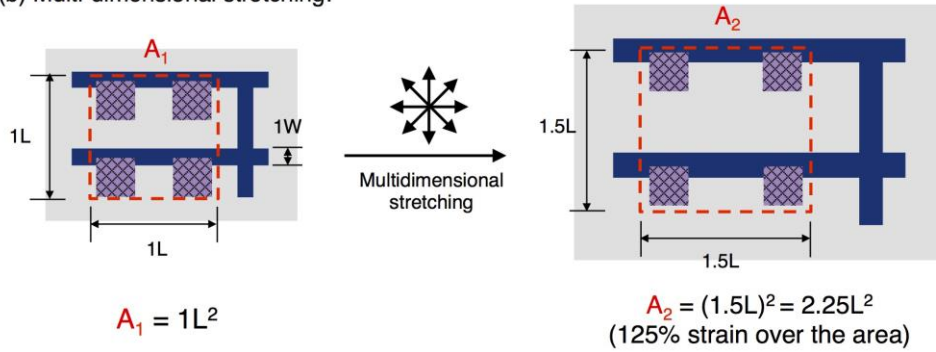


fig. S28. Schematic diagrams illustrating strain calculation for rigid-island devices.

Illustration showing the determination of strain for (a) linear rigid-island arrays under unidirectional stretching vs. (b) two-dimensional arrays under multidimensional stretching.

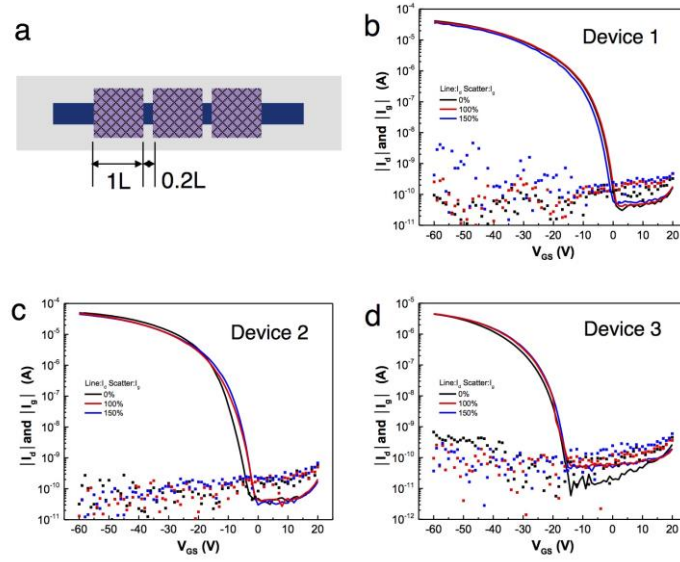


fig. S29. Schematic and transfer characteristics for a 3×1 FET array. (a) Top view schematic of a 3×1 array with a rigid island-to-interconnect ratio of 5:1. (b)-(d) FET transfer characteristics for the 3 devices under 0%, 100%, and 150% strain.

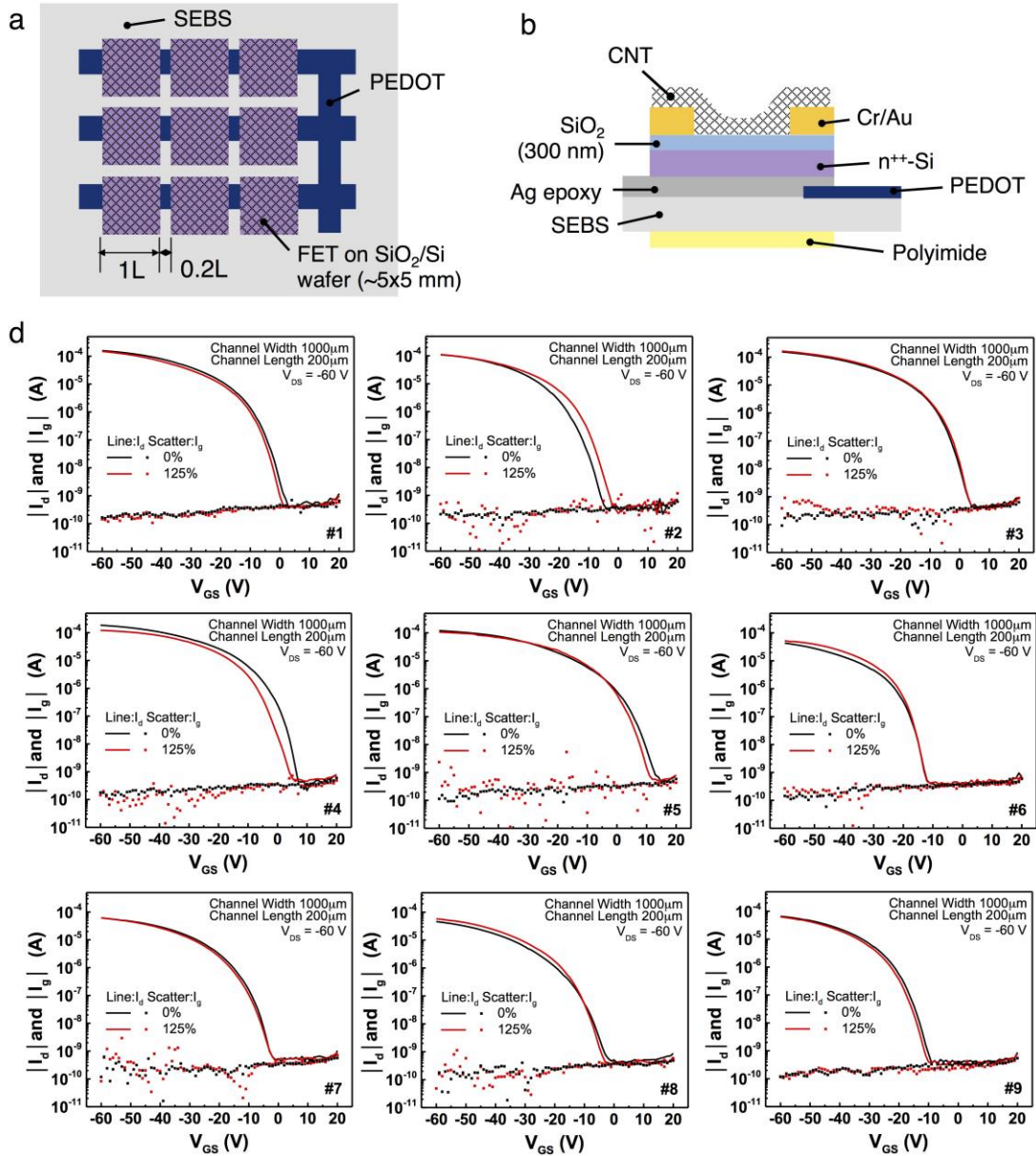


fig. S30. Schematic and transfer characteristics for a 3×3 FET array. (a) Top view and (b) cross-sectional view of the 3×3 rigid-island FET array on SEBS substrate. (c) Transfer characteristics of the FETs under 0% and 125% areal strain under multi-directional stretch.

table S2. Summary of mobility and threshold voltage shift for the 3×3 transistor arrays under 0 and 125% strain. Slight variation in the mobility values (<10%) between array under 0% vs. 125% strain were observed for some of the devices. This could be attributed to the minor fluctuation of the interconnect resistance with strain, which causes the actual gate voltages to vary from the applied value.

Device	Mobility (cm ² /V/s)		Normalized mobility (cm ² /V/s)		V _{th} shift (V)
	0% strain	125% strain	0% strain	125% strain	
1	2.110	2.140	1	1.010	-3.17
2	0.887	0.834	1	0.940	2.83
3	1.300	1.280	1	0.985	2.45
4	2.460	2.290	1	0.931	-2.91
5	0.531	0.528	1	0.994	4.83
6	0.773	0.749	1	0.969	5.65
7	0.998	1.050	1	1.052	-2.00
8	0.670	0.709	1	1.058	4.31
9	1.450	1.430	1	0.986	-1.33

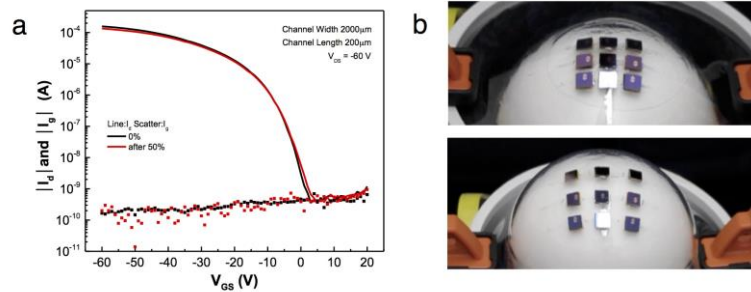


fig. S31. A 3×3 FET array being stretched on a spherical object. (a) Representative transfer characteristic for the rigid island transistor arrays stretched on a curved object. (b) Photographs showing the array at 0% (top) and 125% (bottom) strain.